

Airgap Length Analysis of a 350kW PM-Assisted Syn-Rel Machine for Heavy Duty EV Traction

T. Zou, *Member, IEEE*, D. Gerada, *Senior Member, IEEE*, S. La Rocca, A. La Rocca, A. Walker, G. Vakil, S. L. Arevalo, Z. Xu, M. Cui, A. Bardalai, M. Wang, R. M. Kumar, A. Marfoli, K. Paciura, R. Barden, E. Ernest, S. Zhu, N. Qayyum, A. McQueen, F. Zhang, and C. Gerada, *Senior Member, IEEE*

Abstract—Synchronous reluctance (Syn-Rel) machines with embedded permanent magnets (PMs) are research hotspots in variable speed motor drives due to their robust rotor structure and wide constant power speed range (CPSR). In this paper, the potential of PM-assisted Syn-Rel machine to be next generation heavy duty traction motor solution has been investigated, with special attention put on one key geometric parameter, i.e., airgap length. Careful machine design and optimization has been conducted based on geometric parametrization including airgap length variation, for 15000rpm peak speed and 350kW peak power output. In low speed operations, the influence of airgap length on different torque components has been analyzed in detail based on the frozen permeability method. In field weakening region, the variation trend of several key parameters such as output power, torque ripple, and power losses have been investigated along with airgap length. It is found that with high electric and magnetic loading, reducing the electromagnetic airgap length is not always beneficial. There exists a suitable airgap length value to comprehensively balance torque/power density, cooling capability, efficiency and reliability. Numerical FEA and experimental tests of the prototype are combined to verify the conclusions.

Index Terms—airgap length, synchronous reluctance machine, PM machine, high speed machine, rare earth magnets, high power density.

I. INTRODUCTION

During the last decades, synchronous reluctance (Syn-Rel) machines have drawn ever increasing attentions in variable speed traction applications, mainly due to their PM-free characteristic, high rotor robustness and wide constant power speed range (CPSR) [1-4]. Meanwhile, low energy density permanent magnets (PMs) such as ferrite PMs are still essential for this machine type to form PM-assisted Syn-Rel machines with higher power factor, when practical Volt-Amps (VA) power rating limitation is considered [5-6]. Compared with regular interior PM (IPM) machine, this machine type is characterized with higher magnetic anisotropy and reduced PM usage. In general, the research work in PM-assisted Syn-Rel machines includes analytical modelling [7-10], multi-physics optimization [11], specific case study for industrial applications such as hybrid electric vehicle (HEV) and EV traction [12], as well as high performance control algorithm development [13-14].

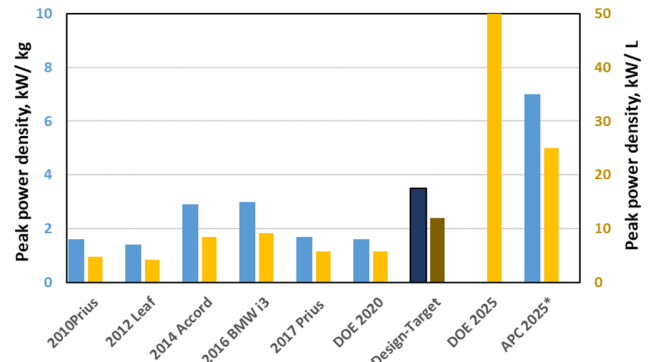


Fig. 1. Peak power density of EV/HEV motors and future roadmaps [21-23].

Due to the relatively complex rotor structure, extensive efforts have been made in analytical sizing of PM-assisted Syn-Rel machines to rapidly establish the relationship between geometric parameters and basic machine performance, such as average torque [7], torque ripple [8], losses [9] and rotor anti-demagnetization capability [10]. Detailed electromagnetic design has been combined with FEA tools to increase calculation accuracy as well as for specific performance requirements [15-16]. In addition, research interests on this machine topology have been extended to multi-physics domains such as mechanical stress on the rotor [17, 18], thermal [19] and noise, vibration, harshness (NVH) aspects [20] for reliability improvement in high speed, high power applications.

Moreover, with ultra-high power density pursued based on ambitious roadmaps made by governments and intensified competition in market of HEVs and EVs [21-23], high energy density magnet material is still preferred in industry. Typical examples are traction machines in Toyota Prius and BMW i3 [24, 25], which basically adopt hybrid topologies of conventional IPM and PM-assisted Syn-Rel machines, with strong NdFeB magnets embedded into the rotors. Prior to this paper work, the authors have been engaged in investigating the potential of typical PM-assisted Syn-Rel machine topologies in high power, heavy duty traction applications, to achieve superior power density of 3.5kW/kg and 12kW/L, compared with typical motor products in market as shown in Fig. 1.

Based on the research work, this paper will focus on the influence of airgap length on machine performance. Normally, the airgap length selection is more dependent on practical manufacturability, and is widely regarded as “the smaller the better” from electromagnetic point of view. However, there are mainly two reasons that the “old-fashioned” design parameter

is brought back to stage. As illustrated in Fig. 1, both DoE 2025 report from the Department of Energy in US [21] and the APC (Advanced Propulsion Centre) Roadmap 2025 [22] in UK have targeted on significant increase in machine's power density (peak value in DoE and continuous value in APC) for EV/HEV within next 5 years. Hence, both "ultra-high speed" and "ultra-high torque density" will be the trend of next generation design. "Ultra-high speed" may bring the possibility of adopting extra rotor sleeve with prestress for Syn-Rel machines (similar with high speed surface-mounted PM machines), and this will increase electromagnetic airgap length. On the other hand, "ultra-high torque density" makes preferred airgap as small as possible, since it is widely accepted that reluctance torque will reduce significantly along with airgap length. Hence, it is necessary to reevaluate airgap length as the most essential design parameter that influences comprehensive performance of PM-assisted Syn-Rel machines.

This paper is organized as follows: The machine performance requirements and design process will be briefly introduced in Section II. Section III will be focused on discussion of the influence of airgap length on torque performance in low speed, high torque operation. Thereafter, Section IV will be devoted to machine performance variation along with airgap length in high speed field weakening region. Further, the multi-physics design process will be introduced with the finalized machine performance highlighted in Section V. Finally, the experimental setup and test results based on the prototype will be given in Section VI.

II. MACHINE TOPOLOGY AND BASIC OPTIMIZATION

Prior to any detailed geometric design, the machine performance towards high power density is first of all highly dependent on effective material properties. In this paper, high performance electrical steel 10JNEX900 and 35HXT780T are adopted for the stator and rotor core, respectively. 10JNEX900 is the state of art 0.1mm Si-Fe steel with low core loss density [26], while 35HXT780T is with high yield strength of over 840Mpa [26, 27], thus suitable to be the lamination material for high speed rotor core. N38EH has been selected as PM material to provide high energy density and guarantee thermal reliability of up to 150°C.

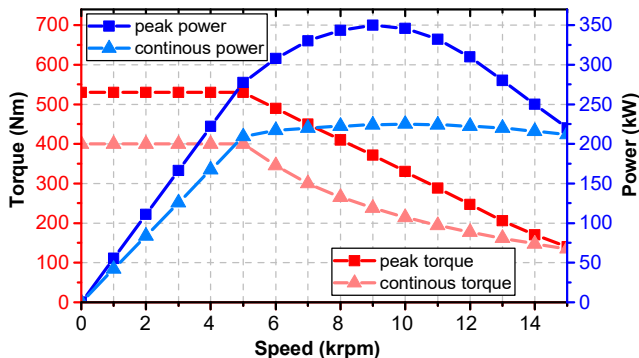


Fig. 2. Targeted torque/ power rating vs. speed for the machine design.

The targeted power and torque-speed curve is given in Fig. 2, with CPSR ratio of 3:1 for continuous operation. At knee point of 5000rpm, rated and peak torque of 400Nm and 530Nm

are required. More detailed design specs limitations are listed in Table I. Six phase winding configuration (no phase shift) has been selected to be compatible with inverter capability.

TABLE I
Performance requirements and design limitation

Item	Value
Max. diameter/ length, mm	350
Max. active mass, kg	60
Max. non-active mass, kg	40
Max. inertia, kg*m ²	0.4
Peak power (30s), kW	350
Continuous power, kW	225
Peak power density, kW/kg	≥3.5
Peak power density, kW/L	≥12
Peak/continuous rms current, A	330/220
DC bus voltage, V	650

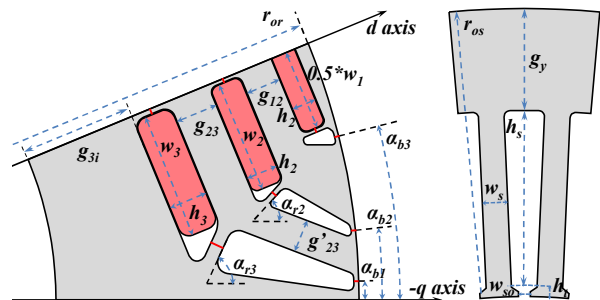


Fig. 3. Parametric rotor and stator modelling with 72-slot, 8-pole combination.

With high power density, high speed pursued, the overall machine development is inherently a multi-physics problem with limited boundary on electromagnetic (EM), thermal and mechanical aspects. Fig. 3 gives the globally parametric rotor and stator topology of the PM-assisted Syn-Rel machine with selected 72-slot, 8-pole combination for detailed design. Initial sizing has been focused on rotor outer radius r_{or} , split ratio and aspect ratio to balance EM performance and rotor mechanical stress. Five PMs located into three layers per pole is configured with w_1 - w_3 , h_1 - h_3 denoting magnet width and height, respectively. In the meanwhile, the gaps g_{12} , g_{23} between PMs and g'_{23} between flux barriers, as well as angle α_{r2} , α_{r2} together determines the q -axis flux path and needs to be synergistically considered. The bridge positions represented by angle α_{b1} , α_{b2} and α_{b3} influence significantly the torque ripple and needs to be carefully designed. Moreover, all the bridges, ribs marked in red also influence significantly the rotor von-Mises stress distribution, together with rotor yoke thickness g_{3i} . Hence, their sizing are also considered for mechanical reliability. On the other hand, the stator core is modelled with parametric yoke, tooth and slot region based on reasonable limitation on magnetic and electric loadings as well as winding loss. It should be noted that the EM design of the machine is based on numerical FEA with ferromagnetic non-linearity fully considered under different levels of magnetic saturation. This is an important basis for the following up airgap length investigation. As the B-H curves of selected stator and rotor core materials are within standard ranges as steel laminations, the conclusions based on airgap length analyses in the following sections could be extended to design cases with other typical materials adopted as well.

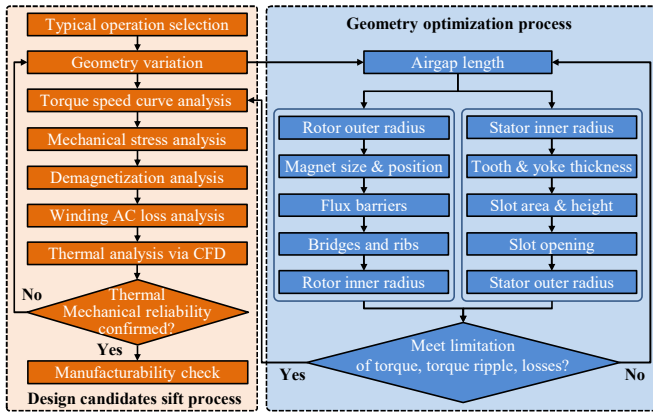


Fig. 4. Design flowchart with airgap variation considered.

The machine development process follows the flowchart as shown in Fig. 4. The airgap length which is normally fixed prior to detailed EM design has been set as additional variable. Due to the complex machine topology, quite a few parameters will influence the output performance in a coupled way, while the research focus in this paper will be the influence of airgap length instead of global optimization. The turn number in series per phase, as an impact factor of both PM flux linkage and dq -axis inductance, has been carefully designed for the targeted torque/power-speed curve. Moreover, the 6-step V-shape skewing with 1.67 degree shifted between neighbouring rotor segments has been applied on the rotor for the reduction of 18th torque ripple harmonic, while the geometric optimization mainly works on 6th and 12th harmonics. In this section, two typical operation points, i.e., 400Nm at 5000rpm and 210kW at 15000rpm, have been selected as case study.

In order to comprehensively investigate the influence of airgap length, the variations of magnet sizes & positions, flux barriers and bridge positions, as well as slot opening have also been considered. Meanwhile, to balance calculation time and efficiency, the rotor outer diameter, stator slot area, tooth and yoke thickness have been sifted with reasonable values. For 5000rpm operation, preprocessing script is imbedded in Jmag-Designer to rapidly secure the lowest rms current and related phase advance angle for 400Nm output torque. For high speed operation, similar but more complex algorithm has been developed with reference to [14] for each machine geometry, featuring a common 210 kW output power and peak line voltage, with focus on reducing the power loss components.

Fig. 5 gives performance comparison of different machine geometries for 400Nm output torque, with winding loss and torque ripple highlighted. In general, it can be concluded that for low speed, high torque operation:

- 1) Torque ripple has an inverse correlation with airgap length;
- 2) Higher airgap length leads to increased winding losses due to higher input current needed;
- 3) Either relatively high PM usage or small airgap length is needed to reduce winding loss;
- 4) With airgap length varying from 0.75 to 1.75mm, similar level of winding loss and torque ripple could be achieved.

While conclusion 2) and 3) are already widely accepted, 1) and 4) provides an insight that the torque performance

reduction due to increased airgap length can be offset by proper rotor design. The PM flux linkage and saliency ratio could be flexibly adjusted by changing the PMs' sizes and positions with a modified airgap length, to maintain the output torque with the same input current and winding loss. Meanwhile, the high torque ripple due to very small airgap is challenging to be alleviated when high electric loading is applied.

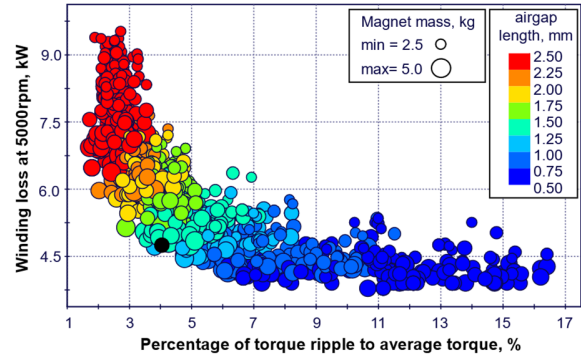


Fig. 5. Variation trends between airgap length, magnet usage, winding loss and torque ripple, for 400Nm, 5000rpm operation.

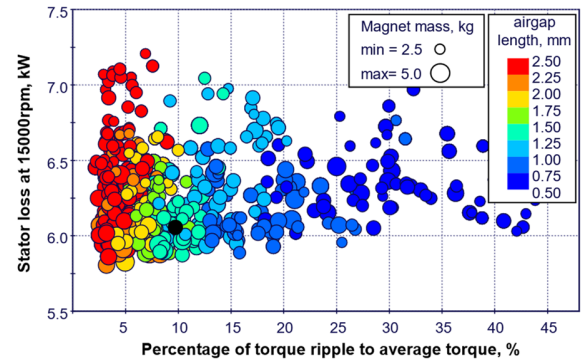


Fig. 6. Variation trends between airgap length, magnet usage, stator loss (copper loss + iron loss) and torque ripple, for 210kW, 15000rpm.

Fig. 6 shows the cases for 210kW, 15000rpm operation, in which the torque ripple follows similar trend along with airgap length compared with that in Fig. 5. It should be noted that both copper and iron loss components are included in stator loss calculation for this high speed operation. Meanwhile, it is interesting to find that larger airgap is not leading to increased stator power losses (copper + iron loss) or PM usage. In other words, with the same limitation of cooling capability or efficiency target, machine designs with large airgap length can achieve the same output power compared with small airgap counterparts, in high speed field weakening operations. By combining Fig. 5 and 6, it can be seen that the design cases with 0.75-1.75mm airgap length could achieve similar output performance & losses for both low and high speed operations, simply at different cost of PM material consumption. Specifically, the down-selected case with 1.0mm airgap length for prototyping is highlighted in black in both Fig. 5 and 6, featuring a balanced compromise between high torque quality, low power losses and magnet usage. Based on the discussion above, airgap length of PM-assisted Syn-Rel machines is worth further investigation to exploit the essence of its influence on machine performance.

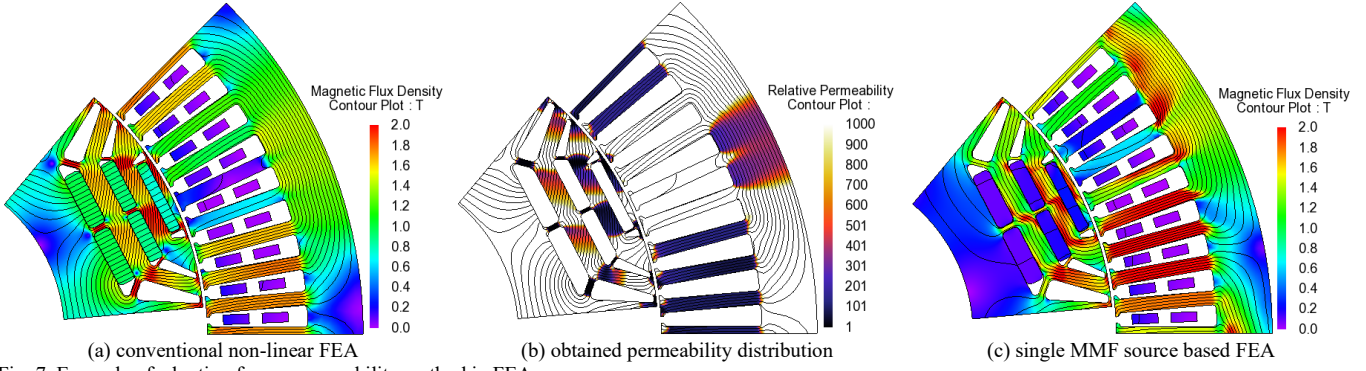


Fig. 7. Example of adopting frozen permeability method in FEA.

III. INFLUENCE OF AIRGAP LENGTH IN MTPA REGION

In this section, variation of different torque components of PM-assisted Syn-Rel machine along with airgap length will be quantitatively investigated, to reveal the nature of how this fundamental parameter would influence the overall torque performance under high electromagnetic loading. It should be noted that the machine has gone through EM optimization based on different values of airgap length for a fair comparison. In each case, the PM flux linkage and winding inductance have been carefully designed so that the machine falls into “the 2nd or 3rd type” capability curves according to [10] as required in Fig. 2. Due to space limitation of the paper, only the optimized machine topology will be discussed as case study in this section, with airgap length variable while other parameters fixed, which can give equivalent insight of how airgap length influences machine performance directly.

In order to separate the influence of airgap length on different torque components, frozen permeability method [28] is applied. Fig. 7(a) shows flux density distribution of the optimized machine topology under maximum torque per ampere (MTPA) operation. It should be noted that the current loading under continuous and peak operation are around 800 A/cm and 1200 A/cm, respectively. With high electromagnetic loading, the stator and rotor core are inevitably under partial saturation, especially in its d -axis (dq -axis reference frame referred to general IPM machines) flux path. Based on Jmag-Designer, the magnetic permeability distribution of iron cores could be globally recorded and applied to further FEA studies with single MMF source, as shown in Fig. 7(b) and (c). With cross-coupling saturation considered, the mathematical model of the machine is written as Eqn. (1)-(3), while all the four torque components are expressed in Eqn. (4)-(7). Both PM torque and reluctance torque contain conventional and cross coupling components as shown in Eqn. (8) and (9).

$$\begin{aligned} \Psi_{PM} &= (\Psi_{PMd}, \Psi_{PMq}) & (1) \\ \Psi_{Id} &= L_d I_d, \quad L_d = (L_{dd}, L_{qd}) & (2) \\ \Psi_{Iq} &= L_q I_q, \quad L_q = (L_{dq}, L_{qq}) & (3) \\ T_{PM-Main} &= p \Psi_{PMd} I_q & (4) \\ T_{PM-Cross} &= -p \Psi_{PMq} I_d & (5) \\ T_{Rel-Main} &= p (L_{dd} - L_{qq}) I_d I_q & (6) \end{aligned}$$

$$T_{Rel-Cross} = p (L_{dq} I_q^2 - L_{qd} I_d^2) \quad (7)$$

$$T_{PM} = T_{PM-Main} + T_{PM-Cross} \quad (8)$$

$$T_{Rel} = T_{Rel-Main} + T_{Rel-Cross} \quad (9)$$

$$T_{Total} = T_{PM} + T_{Rel} \quad (10)$$

In Eqn. (1-10), Ψ_{PM} is the PM flux linkage with both d - and q -axis components due to the cross coupling saturation. Ψ_{Id} and Ψ_{Iq} are flux linkages induced by d - and q -axis current I_d and I_q , respectively. The inductances L_d and L_q which corresponds to armature reaction from I_d and I_q contain both self and mutual components. The PM torque T_{PM} related to PM flux linkage consists of two components, i.e., $T_{PM-Main}$ and $T_{PM-Cross}$. Meanwhile, The reluctance torque led by rotor anisotropy also corresponds to the main part $T_{Rel-Main}$ and cross coupling part $T_{Rel-Cross}$. According to the process shown in Fig. 8 [28], all the flux linkage and inductance values can be obtained for torque calculation. Fig. 9 shows the variation of each torque component along with phase advance angle. The sum of these torque components match very well (error < 0.1%) with the total torque directly from FEA, which validates the effectiveness of this method.

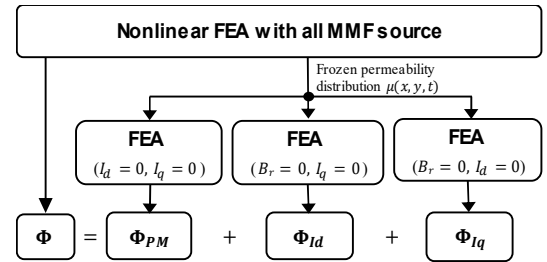


Fig. 8. Decomposition of mathematical model with frozen permeability [28].

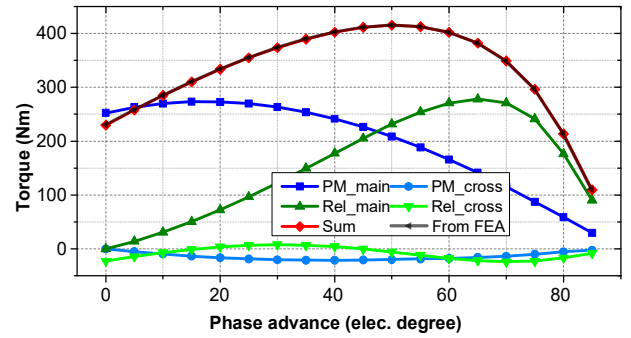


Fig. 9. Variation of different torque components with phase advance.

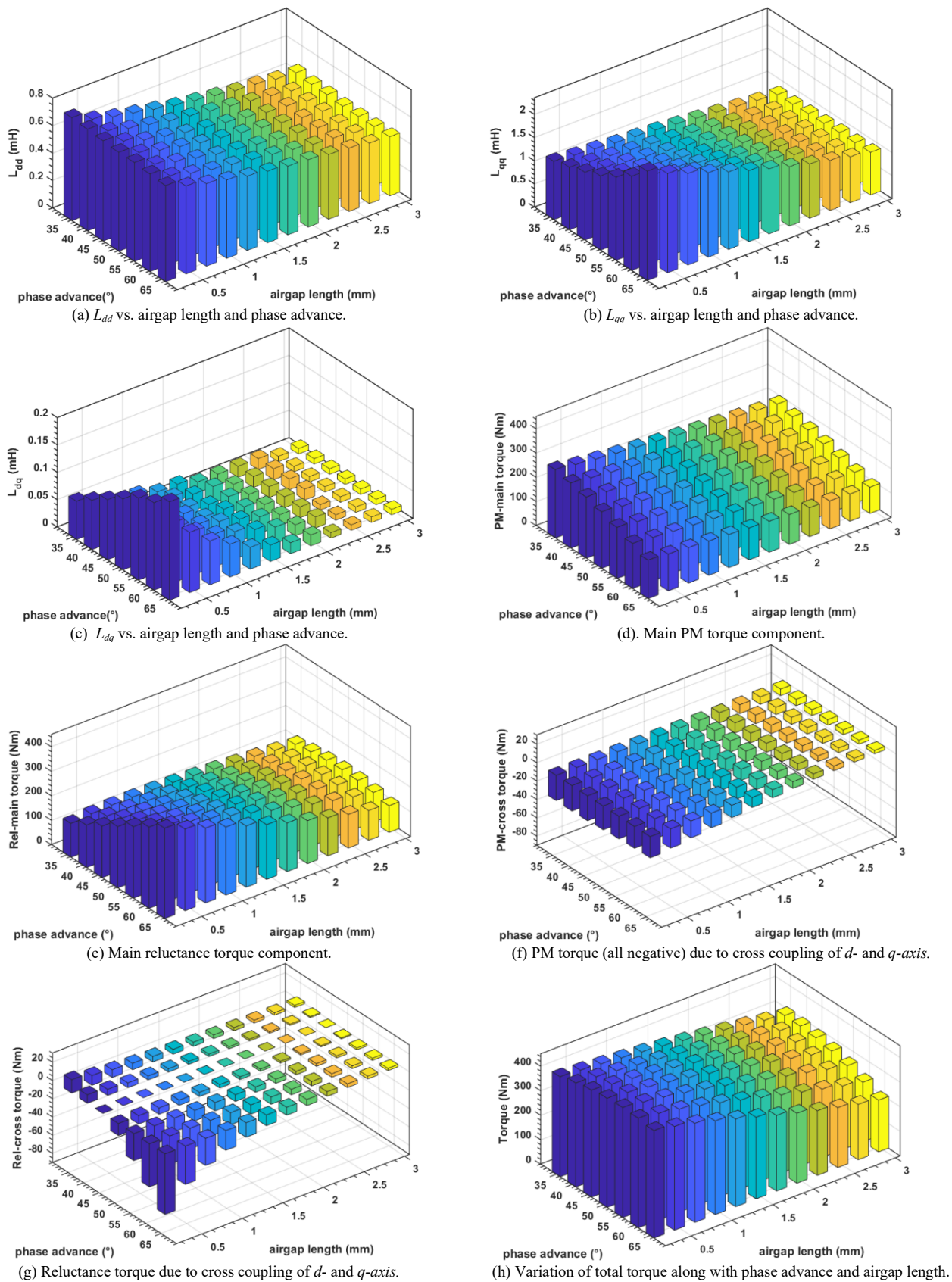


Fig.10. Variation of typical machine parameters along with airgap length and phase advance angle, with rated rms current of 220A.

Then, the variations of machine inductance and torque components along with airgap length are calculated and illustrated in Fig. 10. Fig. 10(a)-(c) give the variation of L_{dd} , L_{qq} , and L_{dq} , along with airgap length and phase advance while phase current is fixed at 220rmsA. All the inductance components are dropping with increase of airgap length. At 50° phase advance, the percentage reduction of L_{dd} , L_{qq} , and L_{dq} when airgap increases from 0.5mm to 2.0mm are 24.2%, 25.0% and 77.8%, respectively. It is interesting to find from Fig. 10(a) that L_{dd} is decreasing along with higher phase advance when the machine becomes less saturated in its main flux path. This is due to more saturated bridges and ribs led by stronger d -axis armature reaction, which would only exist in high speed Syn-Rel machines. Moreover, it should be noted in Fig. 10(c) that with tiny airgap (≤ 0.5 mm), d - and q -axis coupling will be much stronger and lead to obvious negative torque component $T_{Rel - Cross}$. Fig. 10(d)-(e) shows the influence of airgap length on the main PM and reluctance torque. First, it can be clearly seen that for each specific phase advance angle, both torque components reduce along with airgap length. With phase advance of 50°, there are 17.8% and 25.4% reduction of the main PM and reluctance torque respectively, when the airgap is increased from 0.5mm to 2.0mm. This can be easily predicted as higher airgap length always corresponds to reduced PM flux linkage as well as winding inductance.

It should be noted that the main PM torque is less reduced compared with that of the main reluctance torque. According to Eqn. (4) and (6), this is because Ψ_{PM} is less susceptible compared with ($L_{qq}-L_{dd}$), as the magnetic saturation is alleviated with larger airgap. Meanwhile, the high magnetic and electric loading for high power density target will lead to non-negligible cross coupling saturation. This saturation will then introduce calibration of magnetic pole axis. Hence, there will be additional PM torque produced by d -axis current, as well as additional reluctance torque due to mutual inductance between d - and q -axis. In MTPA region, both of these two torque components would be negative and lead to total torque reduction, as can be seen in Fig. 10 (f) and (g). With cross coupling considered, the real PM and reluctance torque reduction when airgap changes from 0.5mm to 2.0mm while phase advance angle remains 50°, is dropped to 13.5% and 23.2%, respectively. The total torque variation is shown in Fig. 10 (h). Correspondingly, The total torque reduction is 19.0%, in which 5.0% drop happens from 0.5mm to 1.0mm airgap increase, and 14.8% drop happens from 1.0mm to 2.0mm airgap increase.

As a summary for the discussion above, with high electromagnetic loading applied to the PM-assisted Syn-Rel machine, the torque performance will not be as significantly deteriorated as assumed when the electromagnetic airgap length increases within reasonable ranges. There are two reasons for this phenomenon. One is, the overall saturation level of the machine is alleviated with larger airgap, so the main PM torque component does not drop much. The other reason is, with very small airgap, the cross-coupling saturation leads to considerable negative torque components which offsets the main torque.

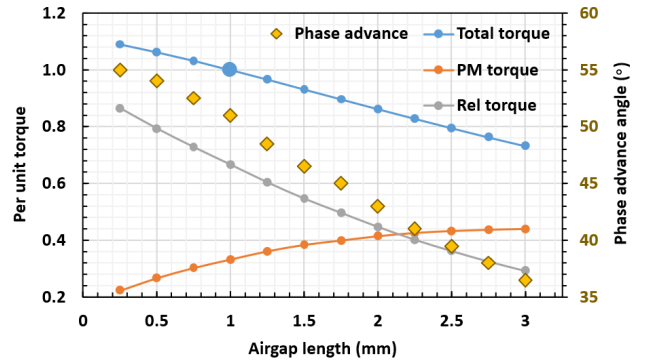


Fig. 11. Influence of airgap length on torque components and optimal phase advance angle. Base torque value is set as the one obtained with 1.0mm airgap.

Meanwhile, the airgap length variation will also influence the optimal phase advance angle that follows MTPA locus. Take the designed machine as example, the suitable phase advance angle reduces from 55° to 36.5° with airgap increasing from 0.25mm to 3.0mm, as shown in Fig. 11. If different phase advance angle is respectively selected to achieve MTPA for each case of airgap length, it is interesting to find that the corresponding PM torque component shows the trend of increase instead of reduction. This is because more q -axis current is applied for MTPA when airgap increases. Hence, the total torque reduction with larger airgap is basically only introduced by loss of reluctance torque component.

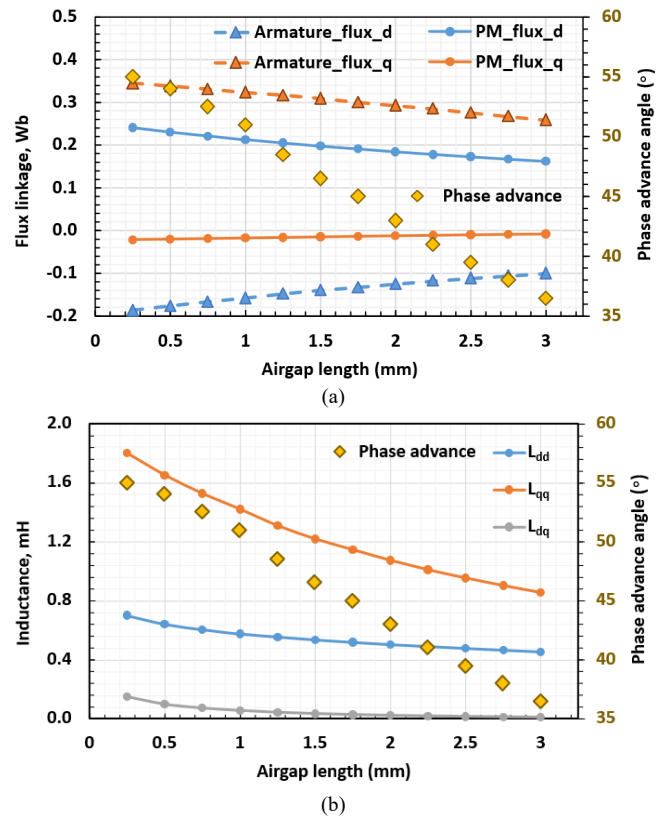


Fig. 12. Influence of airgap length on (a): flux linkage and (b): inductance components based on optimal phase advance angle.

Moreover, the influence of airgap length on flux linkage and inductance components are further illustrated in Fig. 12 following the optimal phase advance angle from Fig. 11. It should be noted that these components are “on-load” ones based on the frozen permeability method. Fig. 12(a) shows that the absolute values of all flux linkage components gradually reduce along with higher airgap length. From Fig. 12(b), it can be seen that the drop of main reluctance torque is attributed by both the reduction of L_{dd} , L_{qq} , and much lower saliency ratio along with larger airgap.

Another performance index which needs to be evaluated along with airgap length variation is the demagnetization of magnets. demagnetization situations based on different airgap length have been analyzed based on most challenging operation points, i.e., inter-phase short circuit at peak torque in MTPA region. As shown in Fig. 13, increase of airgap length will alleviate the risk of demagnetization. It should be noted that the four cases below correspond to the same peak torque value, which means the injected current is higher in cases with higher airgap. Meanwhile, even with higher injected current, the cases with larger airgap still have reduced risky region in terms of demagnetization.

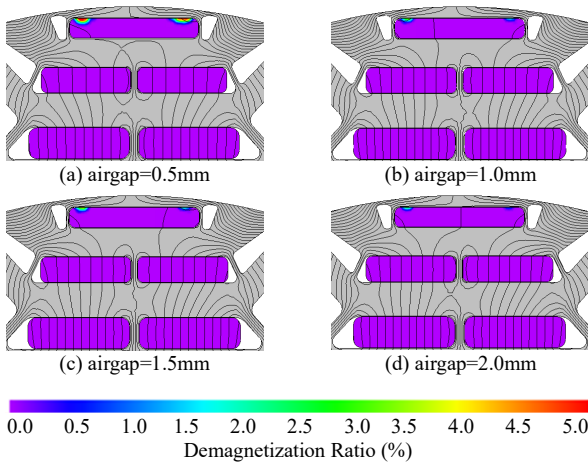


Fig. 13. Distributions of demagnetization after symmetric inter-phase short circuit at peak torque of MTPA region, with different airgap length.

IV. INFLUENCE OF AIRGAP LENGTH IN HIGH SPEED FIELD WEAKENING REGION

This section will be focused on discussion of how airgap length can affect machine performance when kVA limitation is considered. As introduced, the machine has been designed with characteristic current close to rated current. Hence, wide CPSR can be obtained in the whole high speed field weakening region. This is achieved by carefully optimizing machine topology as well as selecting suitable turns in series per phase for windings. For the designed machine, the kVA margin on the drive side is ~35% (maximum power / kVA capability = 0.65) for both continuous and peak operation due to specific inverter configuration.

Fig. 14 shows the values' distribution of airgap length, magnet usage, rms current and phase advance, for 210kW, 15000rpm operation during the topology sifting process

discussed in Section II. It can be seen that with larger airgap, the phase advance angle shows the trend of considerable reduction while effective field weakening can still be achieved. Hence, within a certain range, larger airgap might not necessarily deteriorate the CPSR capability for high power PM-assist Syn-Rel machines.

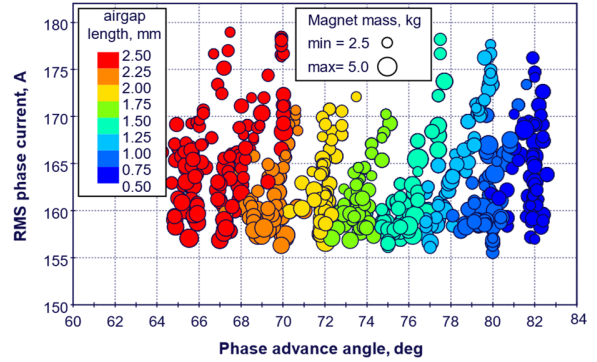


Fig. 14. Variation trends between airgap length, magnet usage, rms current and phase advance angle, for 210kW, 15000rpm operation.

Airgap length is set to be the only geometric variable in the following analysis in this section to more intuitively illustrate its influence in high speed operation, while the other design parameters have been optimized based on the airgap=1.0mm case. In deep field weakening region, the magnetic saturation in the main flux loop of the designed machine is much lower than that of MTPA region. With the increase of airgap length, both PM flux linkage and d-axis inductance will reduce, and thus affecting the value of characteristic current. Meanwhile, the saliency ratio which also affects maximum power, will change along with airgap length as well. The power-speed curve of the machine is then analytically derived based on the kVA limitation and machine's simplified mathematical model, in which the PM flux linkage, d - and q -axis inductance matrix are obtained from MotorCAD. Based on analytical equations, Fig. 15 gives the comparison results of power-speed curves under continuously rated current with different airgap length. In this figure, airgap length is the only geometric variable, which gives insight on how it will influence the output power capability of the machine based on the same kVA limitation. It can be seen that the maximum power only slightly drops along with increase of airgap length (1.7% drop from 0.25mm to 1.5mm, 3.9% drop from 1.5mm to 3.0mm). Hence, the influence of airgap length in field weakening operation is less than that in MTPA region from output power point of view.

Meanwhile, it should be noted that only the fundamental voltage generated by PM flux linkage and d -, q -axis armature reaction are considered in field weakening derivation as shown in Fig. 15. With strong armature reaction, there are rich harmonics of inductance with higher orders. These inductance harmonics will produce considerable flux linkage and voltage harmonics, which cannot be simply “weakened” by injecting d -axis current. Hence, the resultant voltage distortion will deteriorate field weakening performance. Further lower fundamental voltage limit has to be followed by putting more demagnetizing current, and output power will therefore be

reduced. Fig. 16 shows more practical output power capability obtained from numerical FEA with all inductance harmonics and voltage distortion considered. It can be seen that the achievable output power drops significantly with tiny airgap. With 0.25mm and 0.5mm airgap based on the specific machine geometry design, it is even impossible to restrict the peak value of line voltage to be within DC bus due to its significant harmonic components under peak speed. Hence, the practical maximum power under fixed kVA will first increase and then reduce along with airgap length. Although this conclusion drawn from Fig. 16 cannot be generalized as other geometric parameters are fixed with only the airgap length varying, it still provides clear insight that with high electromagnetic loading applied to the PM-assisted Syn-Rel machine targeting on high power density, relatively larger airgap might be beneficial for machine design in field weakening operation.

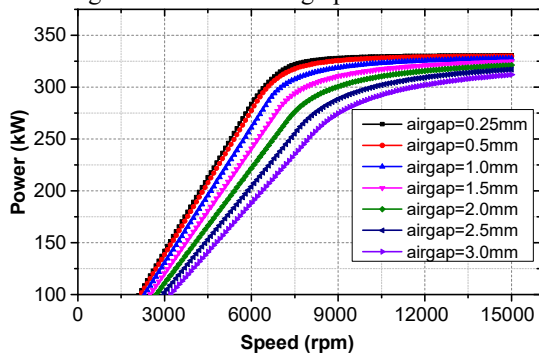


Fig. 15. Power-speed curves based on simplified PM flux linkage and dq -axis inductance matrix of the machine.

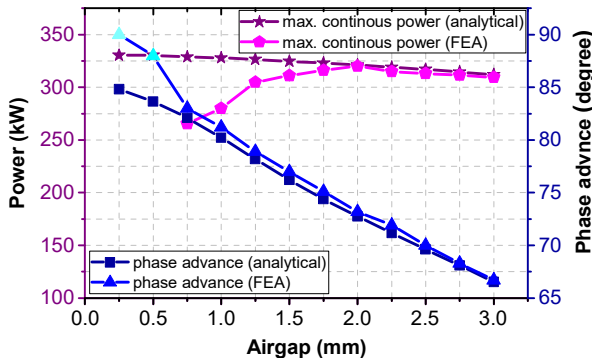


Fig. 16. Comparison of the output power at peak speed based on mathematical modelling and numerical FEA of the machine with variable airgap length.

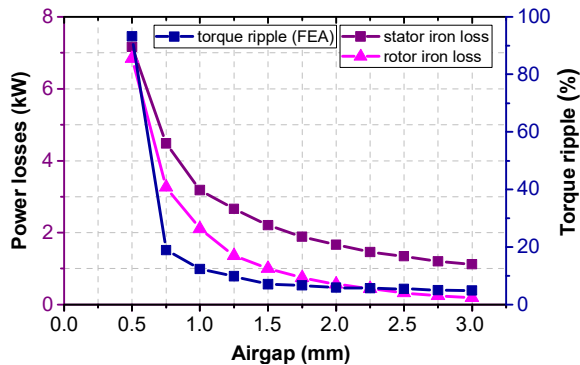


Fig. 17. Influence of airgap length on iron loss and torque ripple in field weakening region.

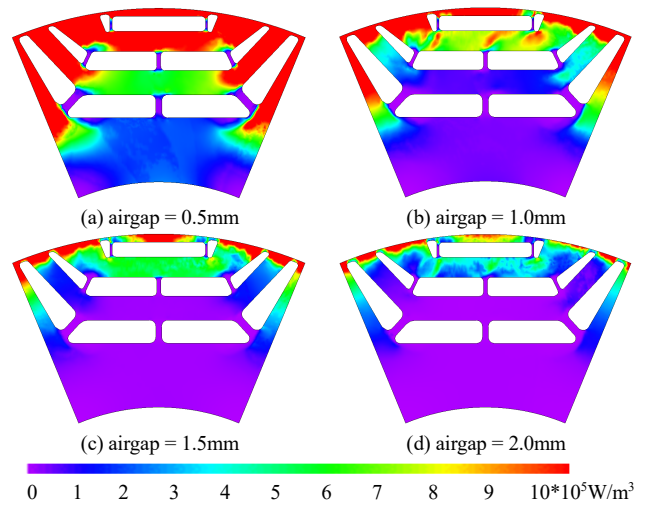


Fig. 18. Influence of airgap length on rotor iron loss distribution at 15000rpm.

Besides, small airgap may also bring challenges in terms of higher iron loss and increased torque ripple in high speed region, as shown in Fig. 17. It should be specially emphasized that cooling of the rotor might be quite challenging for high speed EV motors. Hence, It is important to reduce the rotor loss at the electromagnetic design stage to acceptable level. Based on this consideration, too small airgap needs to be avoided, as the rotor iron loss would be too high to be effectively reduced by optimizing other design parameters. For the specific design with maximum speed operation, the stator and rotor iron loss are reduced significantly by 55% and 70% with airgap changing from 0.5mm to 1.0mm. Similar conclusion also works for the torque ripple. Fig. 18 further illustrates the rotor iron loss distribution from FEA, which clearly reflects much higher iron loss density induced by stronger armature reaction with small airgap.

V. MULTI-PHYSICS DESIGN SUMMARY

In this section, the design results based on the multi-physics optimization will be briefly introduced. Detailed configuration and performance of the optimized machine based on the selected 1.0 mm airgap length are summarized in Table II. As discussed, the split ratio and aspect ratio of the machine have been carefully selected to balance the design challenges on electromagnetic performance, rotor mechanical reliability, as well as cooling capability featuring the end winding oil spray. Moreover, appropriate margin has been maintained on output torque & power compared with requirements in Table I.

Fig. 19 gives the mechanical stress distribution of the optimized rotor at rotation speed of 16500rpm, 10% higher than peak operation speed of 15000rpm. It can be seen that >15% margin is achieved considering the material yield strength of 840MPa. Fig. 20 shows the temperature distribution of the machine based on CFD analysis with integrated oil cooling (equivalent oil flow rate is ~8L/min). Corresponding power losses are obtained based on 160Nm, 15krpm continuous operation. It can be seen that based on oil spray in the end winding and hollow shaft region, the highest temperature rise corresponds to enough safety margin, while axially middle part

of the stator windings is the hot spot. Fig. 21 shows the efficiency map obtained from Jmag under 650V DC bus voltage and 330rmsA peak current. It can be seen that the required torque-speed range can be satisfied based on the optimized machine.

TABLE II
DESIGN SUMMARY OF THE OPTIMIZED MACHINE BASED ON FEA

Parameters	Values
Stator outer diameter, mm	288.0
Rotor outer diameter, mm	190.0
Axial length, mm	155.0
Airgap length, mm	1.0
Slot & pole combination	72 & 8
Winding configuration	6-phase, 2-layer lap winding
Turns per coil	6
Turns in series per phase	18
Peak power with 330rmsA, kW	378.0
Continuous power with 220rmsA, kW	279.0
Peak torque with 330rmsA, Nm	580.1
Continuous torque with 220rmsA, Nm	410.0
DC winding loss at 220rmsA, kW	4.1
Total/DC winding loss ratio at 15000rpm	2.1
Stator & rotor iron loss at 210kW 15krpm, kW	2.6 & 1.7
Mass of stator core, rotor core and magnets	28.1, 16.6, 3.8
Stator & rotor core material	10JNEX900 & 35HXT780T

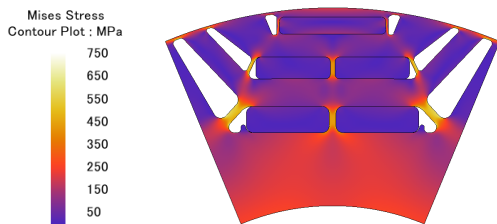


Fig. 19. Von Mises stress of optimized rotor at 16500rpm (10% over peak speed). Maximum local stress = 722.6MPa.

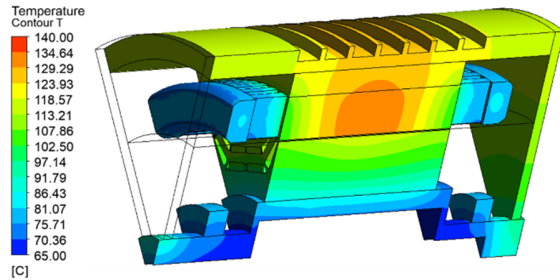


Fig. 20. Temperature distribution of the machine with integrated oil cooling.

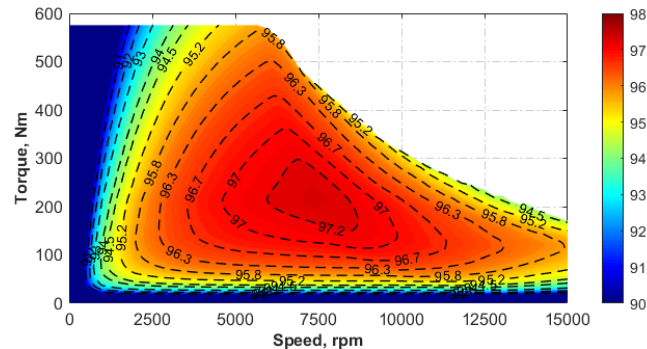


Fig. 21. Efficiency map of the finalized machine design with 650V DC bus voltage and 330rmsA peak current.

VI. PROTOTYPE AND EXPERIMENTAL VALIDATION

Following the finalized design as summarized in Table II, a prototype machine with integrated inverter and cooling unit has been manufactured. Fig. 22 shows the stator and rotor stacks, with the airgap length selected as 1.0mm. 6-step V-shape step skewing is applied to the rotor to alleviate both torque ripple and NVH issue. Fig. 23 illustrates the test bench setup for static torque measurement with rotor locking mechanism. Fig. 24 gives the tested line back-EMF waveforms at 2000rpm, which matches well with simulation results.

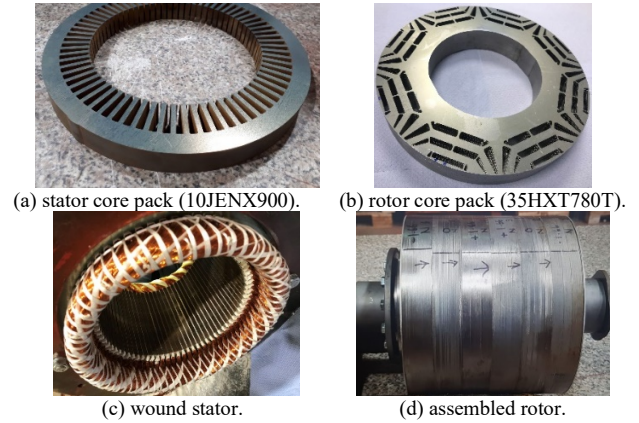


Fig. 22. Components of the prototype machine during assembling process.

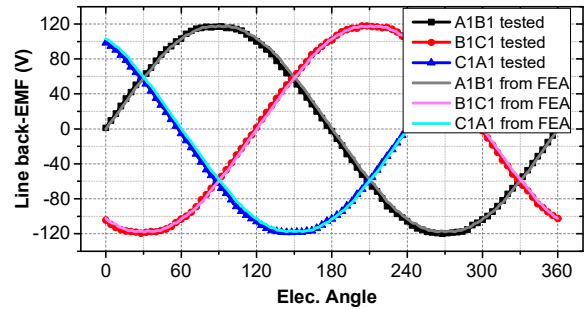


Fig. 23. Comparison of simulated and tested line back-EMF waveforms under 2000rpm.

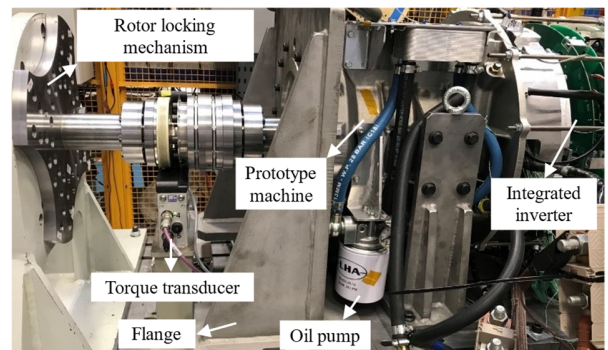


Fig. 24. Test rig set up for static torque measurement.

The static torque is measured by feeding DC current into the phase windings with the rotor locked at different angular positions, as illustrated in Fig. 25. With the current fed into phase A₁ and flowing out of Phase B₁ and C₁ in parallel. The second set of windings are then connected in series with the

first, with the individual phases connected in the same way. The established synthetic current vector is always aligned with axis of Phase A₁ and A₂. The rotor position can then be flexibly adjusted with reference to the current vector, which equivalently corresponds to different phase advance angle. On the other hand, the equivalent operation condition could be easily configured in FEA for comparison.

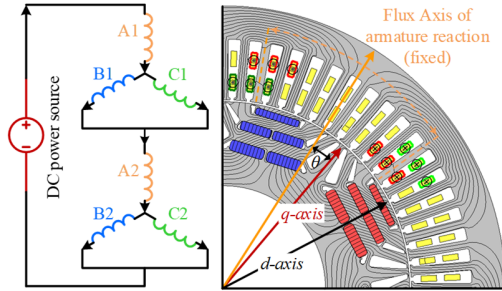


Fig. 25. Illustration of static torque measurement.

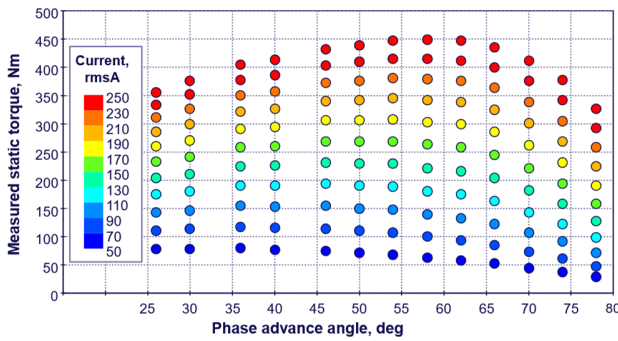


Fig. 26. Measured static torque values along with equivalent rms current and phase advance angle.

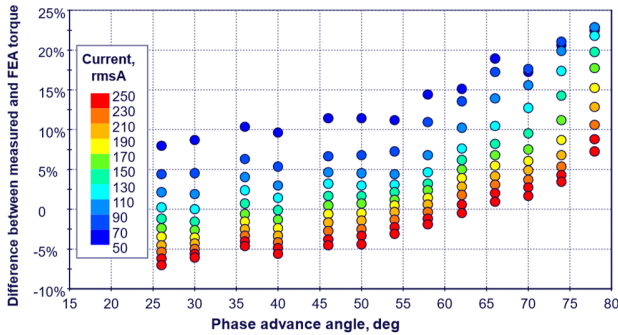


Fig. 27. Percentage difference between measured and simulated torque values, calculated by (measured torque - simulated torque) / simulated torque.

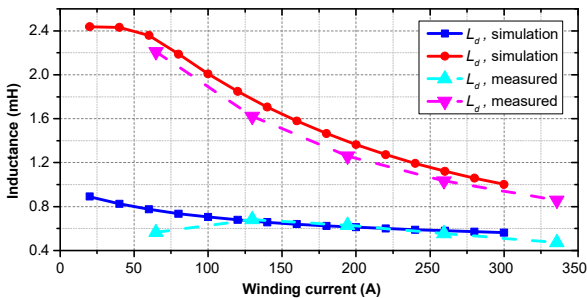


Fig. 28. Comparison of inductance values from experiment and simulation.

Fig. 26 and 27 give the measurement results and its difference with simulation values. As can be seen there are basically three regions where the difference is higher than 5%. With low current the torque difference tends to be higher due to the influence of less accurate torque transducer calibration. With high phase advance angle, the torque difference also becomes higher. This is due to limited accuracy of the rotor locking mechanism, which leads to “amplified” error in equivalent field weakening regions where torque performance is more sensitive to variation of phase advance angle. Moreover, with high rms current and low phase advance angle, the measured torque is lower than the simulated values. This is due to heavy magnetic saturation which leads to more biased practical B-H curve of the stator core compared with its original datasheet used in FEA. Apart from these three regions, the torque measurement matches well with simulation results, and the forgoing analysis can be validated.

Moreover, The rotor locking mechanism has also been used for measurement of winding inductance. By locking the rotor at *d*- and *q*-axis respectively, the *d*- and *q*-axis inductance have been tested based on time stepping response method. Different DC step voltage values have been applied to the windings connected exactly as shown in Fig. 25. The measured data is further compared with corresponding simulation values as shown in Fig. 28. Although it is not possible to further extract different inductance components with cross-coupling effect considered, the consistency of tested and simulated results in Fig. 28 is still acceptable to indirectly validate the research conclusions in Section III.

VII. CONCLUSION

This paper has investigated the influence of electromagnetic airgap length on performance of PM-assisted Syn-Rel machines for high-power, heavy-duty traction application. This “old-fashioned” basic parameter needs to be reevaluated as it influences the trend of machine development towards both high torque density and high speed, featuring the ambitious roadmaps of next generation high-power density drive systems. It has been found that with high performance ferromagnetic material and high thermal loading, the airgap length is not a simple “the smaller the better” case which is widely assumed from electromagnetic point of view. In low-speed high torque operations, the influence of airgap length on different torque components has been analyzed in detail based on the frozen permeability method. It has been found that due to compensation effect of these torque components, the rated torque is only dropped by 6.8% and 13.8% with the airgap length increasing from 1.0mm to 1.5mm and 2.0mm, which is not as significant as assumed. In high-speed high-power region, the variation trend of several key machine parameters such as output power, torque ripple, and power losses have been investigated along with airgap length. It has been found that relatively larger airgap will not deteriorate the machine’s output power capability, while tiny airgap (<0.5mm) may lead to much increased design challenges in terms of lower field weakening capability, high-power losses, and torque ripple. Overall, it can be concluded that with state of art magnetic material properties

and manufacturing technology, relatively larger (between 1.0mm to 2.0mm) electromagnetic airgap can be adopted in PM-assist Syn-Rel traction machines to achieve overall optimized performance, featuring high speed, high power density, reduced core losses as well as torque ripple. This conclusion also provides the insight that rotor sleeve with high mechanical strength can be adopted for high speed, reluctance type traction machines.

VIII. ACKNOWLEDGEMENT

The authors would like to thank POWERSYS for providing JMAG software, as FEA packages for electric machine optimization, and their support to carry out this study.

REFERENCES

- [1] T. Matsuo and T. A. Lipo, "Rotor design optimization of synchronous reluctance machine," in *IEEE Transactions on Energy Conversion*, vol. 9, no. 2, pp. 359-365, June 1994.
- [2] A. Vagati, M. Pastorelli, G. Francheschini, and S. Petrache, "Design of low-torque-ripple synchronous reluctance motors," *IEEE Trans. Ind. Appl.*, vol. 34, no. 4, pp. 758-765, Jul./Aug. 1998.
- [3] N. Bianchi, S. Bolognani, D. Bon and M. Dai Pr , "Torque Harmonic Compensation in a Synchronous Reluctance Motor," in *IEEE Transactions on Energy Conversion*, vol. 23, no. 2, pp. 466-473, June 2008.
- [4] R. Moghaddam and F. Gyllensten, "Novel High-Performance SynRM Design Method: An Easy Approach for A Complicated Rotor Topology," in *IEEE Transactions on Industrial Electronics*, vol. 61, no. 9, pp. 5058-5065, Sept. 2014.
- [5] Y. Wang, D. M. Ionel, M. Jiang and S. J. Stretz, "Establishing the Relative Merits of Synchronous Reluctance and PM-Assisted Technology Through Systematic Design Optimization," in *IEEE Transactions on Industry Applications*, vol. 52, no. 4, pp. 2971-2978, July-Aug. 2016.
- [6] M. Barcaro, N. Bianchi and F. Magnussen, "Permanent-Magnet Optimization in Permanent-Magnet-Assisted Synchronous Reluctance Motor for a Wide Constant-Power Speed Range," in *IEEE Transactions on Industrial Electronics*, vol. 59, no. 6, pp. 2495-2502, June 2012.
- [7] B. Boazzo, A. Vagati, G. Pellegrino, E. Armando and P. Guglielmi, "Multipolar Ferrite-Assisted Synchronous Reluctance Machines: A General Design Approach," in *IEEE Transactions on Industrial Electronics*, vol. 62, no. 2, pp. 832-845, Feb. 2015.
- [8] N. Bianchi, M. Degano and E. Fornasiero, "Sensitivity Analysis of Torque Ripple Reduction of Synchronous Reluctance and Interior PM Motors," in *IEEE Transactions on Industry Applications*, vol. 51, no. 1, pp. 187-195, Jan.-Feb. 2015.
- [9] H. Mahmoud, G. Bacco, M. Degano, N. Bianchi and C. Gerada, "Synchronous Reluctance Motor Iron Losses: Considering Machine Nonlinearity at MTPA, FW, and MTPV Operating Conditions," in *IEEE Transactions on Energy Conversion*, vol. 33, no. 3, pp. 1402-1410, Sept. 2018.
- [10] A. Vagati, B. Boazzo, P. Guglielmi and G. Pellegrino, "Design of Ferrite-Assisted Synchronous Reluctance Machines Robust Toward Demagnetization," in *IEEE Transactions on Industry Applications*, vol. 50, no. 3, pp. 1768-1779, May-June 2014.
- [11] Y. Wang, D. M. Ionel and D. Staton, "Ultrafast Steady-State Multiphysics Model for PM and Synchronous Reluctance Machines," in *IEEE Transactions on Industry Applications*, vol. 51, no. 5, pp. 3639-3646, Sept.-Oct. 2015.
- [12] N. Bianchi, S. Bolognani, E. Carraro, M. Castiello and E. Fornasiero, "Electric Vehicle Traction Based on Synchronous Reluctance Motors," in *IEEE Transactions on Industry Applications*, vol. 52, no. 6, pp. 4762-4769, Nov.-Dec. 2016.
- [13] E. Trancho *et al.*, "PM-Assisted Synchronous Reluctance Machine Flux Weakening Control for EV and HEV Applications," in *IEEE Transactions on Industrial Electronics*, vol. 65, no. 4, pp. 2986-2995, April 2018.
- [14] S. Wang, J. Kang, M. Degano, A. Galassini and C. Gerada, "An Accurate Wide-Speed Range Control Method of IPMSM Considering Resistive Voltage Drop and Magnetic Saturation," in *IEEE Transactions on Industrial Electronics*, vol. 67, no. 4, pp. 2630-2641, April 2020.
- [15] M. Degano *et al.*, "Optimised Design of Permanent Magnet Assisted Synchronous Reluctance Machines for Household Appliances," in *IEEE Transactions on Energy Conversion*, doi: 10.1109/TEC.2021.3076675.
- [16] T. Zou *et al.*, "Influence of Airgap Length on Performance of High Power PM-Assisted Syn-Rel Machines," *2020 IEEE Energy Conversion Congress and Exposition (ECCE)*, 2020, pp. 1357-1363.
- [17] M. D. Nardo, G. L. Calzo, M. Galea and C. Gerada, "Design Optimization of a High-Speed Synchronous Reluctance Machine," in *IEEE Transactions on Industry Applications*, vol. 54, no. 1, pp. 233-243, Jan.-Feb. 2018.
- [18] P. B. Reddy, A. M. El-Refaie, S. Galioto and J. P. Alexander, "Design of Synchronous Reluctance Motor Utilizing Dual-Phase Material for Traction Applications," in *IEEE Transactions on Industry Applications*, vol. 53, no. 3, pp. 1948-1957, May-June 2017.
- [19] Y. Shi, J. Wang and B. Wang, "Transient 3-D Lumped Parameter and 3-D FE Thermal Models of a PMASynRM Under Fault Conditions With Asymmetric Temperature Distribution," in *IEEE Transactions on Industrial Electronics*, vol. 68, no. 6, pp. 4623-4633, June 2021.
- [20] Y. Lu, *et al.*, "Electromagnetic Force and Vibration Analysis of Permanent-Magnet-Assisted Synchronous Reluctance Machines," in *IEEE Transactions on Industry Applications*, vol. 54, no. 5, pp. 4246-4256, Sept.-Oct. 2018.
- [21] 2020 Annual Merit Review Report, Vehicle Technologies Office (VTO), Department of Energy (DOE), USA. June 2020. [Online] Available: <https://www.energy.gov/eere/vehicles/downloads/2020-annual-merit-review-report>.
- [22] N. Jackson, B. Mecrow, *et al.*, "Electric Machines Roadmap 2020", Advanced Propulsion Centre (APC), UK. Feb 2021, [Online] Available: <https://www.apcuk.co.uk/technology-roadmaps/>.
- [23] T. Burrell, *et al.*, "Electrical Performance, Reliability Analysis, and Characterization", DOE Vehicle Technologies Office Annual Merit Review, USA. June 2017.
- [24] S. Sano, T. Yashiro, K. Takizawa, T. Mizutani, "Development of New Motor for Compact-Class Hybrid Vehicles", *World Electric Vehicle Journal*. 2016; 8(2): 443-449.
- [25] J. Merwerth, J. Halbedel, G. Schlangen, "Electrical Drive Motor for a Vehicle," U. S. Patent 20120267977A1, Apr. 25, 2012.
- [26] D. Gerada, A. Mebarki, N. L. Brown, C. Gerada, A. Cavagnino and A. Boglietti, "High-Speed Electrical Machines: Technologies, Trends, and Developments," in *IEEE Transactions on Industrial Electronics*, vol. 61, no. 6, pp. 2946-2959, June 2014.
- [27] Nippon Steel, "Electrical steel sheets," D003jec datasheet, 2019. [Online] Available:https://www.nipponsteel.com/product/catalog_download/pdf/D003jec.pdf.
- [28] K. Yamazaki and M. Kumagai, "Torque analysis of interior permanent-magnet synchronous motors by considering cross-magnetization: variation in torque components with permanent-magnet configurations," in *IEEE Transactions on Industrial Electronics*, vol. 61, no. 7, pp. 3192-3201, July 2014.

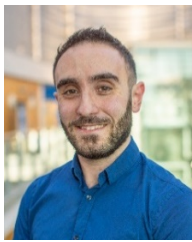


Tianjie Zou (S'15-M'18) received Ph.D. degree in 2018 in electrical engineering, from Huazhong University of Science and Technology, China. In 2018, Dr. Zou joined the University of Nottingham, UK, as a research fellow within the Power Electronics, Machines and Control (PEMC) Group. In 2020, he was awarded tenure-track Nottingham Research Fellowship. He is currently an Assistant Professor within Department of Electrical and Electronics Engineering, University of Nottingham. His main research interests include multi-physics design and intelligent control of electric machines. with special attention on development of high-speed, high-power PM and reluctance machines for electrified transportation.



David Gerada (Senior Member, IEEE) received the Ph.D. degree in high-speed electrical machines from the University of Nottingham, Nottingham, U.K., in 2012. He was with the Research and Development Department, Cummins, Stamford, U.K., first as an Electromagnetic Design Engineer from 2007 to 2012 and then as a Senior Electromagnetic Design Engineer and Innovation Leader from 2012 to 2016. In 2016, he joined the University of Nottingham, where he is currently a Principal Research Fellow, responsible for developing state-of-the-art electrical

machines for future transportation which push existing technology boundaries while propelling the new technologies to higher technology readiness levels. Dr. Gerada is a Fellow of the Institution of Engineering and Technology and a Chartered Engineer in the U.K.



Salvatore La Rocca received the BEng and MEng degrees in Energy and Nuclear Engineering from the University of Palermo (Italy) in 2011 and 2014 respectively; he also received the Ph.D. degree in Mechanical Engineering from the University of Nottingham (U.K.) in 2019. He is a Research Fellow with the Power Electronics, Machines and Control (PEMC) Research Group in the Faculty of Engineering at the University of Nottingham. His research field is the thermo-mechanical modelling and design of high power dense electrical machines

for aerospace, industrial and automotive application.



Antonino La Rocca received his Ph.D. degree from Department of Mechanical, Materials and Manufacturing Engineering Department, University of Nottingham, UK, in 2016. He is a Research Fellow in the Fluids and Thermal Engineering Research Group and the Power Electronics, Machines and Control Research Group in the Faculty of Engineering at the University of Nottingham. His research field is the thermo-mechanical modelling and design of high speed and high power dense electrical machines, power electronics and battery

packs for advanced generation and propulsion systems by the use of Lumped Parameters Thermal networks (LPTN) and Computational Fluid Dynamics (CFD) and FEA.



Adam Walker (Member, IEEE) received the Ph.D. degree in electrical machines design from the University of Nottingham, Nottingham, U.K., in 2016. Previously, he was a Research Associate with the University of Nottingham, where he is currently an Assistant Professor of Electrical Machines and Drives with the Power Electronics Machines and Control Group. His main research interests include electrical machines for traction applications, both personal vehicle and heavy-duty vehicles, but is also interested in thermal management of machines and

design of passive magnetic components.



Gaurang Vakil received the Ph.D. degree in variable speed generator design for renewable energy applications from the Power Electronics, Machines and Drives Group, IIT Delhi, New Delhi, India, in 2016. He subsequently worked as a Research Associate with the Power Electronics, Machines and Controls Group, University of Nottingham, Nottingham, U.K., where he is currently an Associate Professor with the Department of Electrical and Electronics Engineering in 2016. His main research interests

include design and development of high-performance electrical machines and magnetic material characterization.



Saúl López Arevalo received the Ph.D. degree in electrical engineering from the University of Nottingham, Nottingham, U.K., in 2008. From 1998 to 2000, he was a part-time Lecturer with the National Polytechnic Institute, Mexico City and was a Project Engineer with the Mexican Petroleum Institute, Mexico City. He is currently Lecturer in Power Electronics Systems at the National Polytechnic Institute, Mexico City. His research interests are matrix converters, modulation and control strategies, and variable-speed drive systems.



Zeyuan Xu received the Ph.D. degree in mechanical engineering from the University of Manchester, Manchester, U.K., in 2002. He subsequently worked as a Research Fellow at UMIST, Brunel University, and University of Nottingham. He is currently a Principal Research Fellow in thermo-mechanical design of high speed electrical machines within the PEMC group at University of Nottingham, Nottingham, U.K. His main research interests include turbulent thermo-fluid flow, heat transfer enhancement, and thermal management of advanced

electrical machines and power electronics.



Mengmeng Cui was born in Hubei, China. She received the B.Sc. degree in 2016 in electrical and electronic engineering, from Zhejiang Sci-Tech University, China. She started her research career in design and analysis of PM and reluctance type electric machines as a master student in 2016, and then as Ph.D. student, both in Huazhong University of Science and Technology, China. She is currently a PhD student within Power Electronics, Machines and Control Group, University of Nottingham, U.K.



Anuvav Bardalai (M'19) received the Ph.D. degree in 2019 and currently working as a Research Fellow in Electrical Machines at the University of Nottingham, Nottingham, U.K. His expertise is in modelling, analysis, and mitigation of ac losses in high-frequency rotating electrical machines and his research interests include design and analysis of high-speed electrical machines for applications related to traction and aerospace.



Meiqi Wang (Member, IEEE) received the B.Eng. degree in electrical engineering from the Northeast Electric Power University, Jilin, China, in 2014. During 2014 to 2017, she was a joint training master student in electrical engineering of Tsinghua University, Beijing, and Northeast Electric Power University, Jilin, China. She is currently pursuing the Ph.D. degree with the Power Electronics, Machines and Control (PEMC) Group, University of Nottingham, Nottingham, U.K. Her research interests include power electronics and advanced control

techniques for high-speed permanent magnet machines and synchronous reluctance machines for transportation electrification.



R. M. Ram Kumar received the B.Tech. degree in electrical engineering from RMD Engineering College, Chennai, India, in 2014. He is currently pursuing his M.Tech. and Ph.D. dual degree from the Indian Institute of Technology Bombay, Mumbai, India. His research interests are design of high-speed motors for electric vehicles, PM assisted synchronous reluctance motors, modelling and control of motors.



Alessandro Marfoli received the M.Sc. in Electrical Engineering from the University of Pisa, Italy, in 2015, and the Ph.D. degree in electrical machine design from the University of Nottingham (UK) in 2020 where he is currently a Research Fellow. His main research interests include modelling, analysis and optimization of electrical machines.



Krzysztof Paciura graduated in Industrial Power Electronics Department, Warsaw University of Technology, Poland in 1996. He spent the first 13 Years of his career in South Africa and Malaysia, working on breakthrough technologies in Hybrid Power Generation applications. He joined Cummins in 2010, working on developing the Hybrid Permanent Magnet Motor and Power Electronics inverter. In 2012, he became a Technical Project Leader managing multiple projects in conjunction with the University of Nottingham. Between 2014 -

2022 he led Power electronics and Electrical Machine developments on several UK government-funded projects, pushing boundaries in products, technologies and components supply chain developments.



Richard Barden received MEng (Hons) degree in Mechanical Engineering from University of Nottingham (UK) in 2001. In 2012, he joined Cummins Generator Technologies as a Design Draughter progressing to Mechanical Design Engineer focused on Motor Generator Electrical Machines for Hybridisation of Heavy-Duty Truck/Bus application. 2016-17 he supported Cummins' newly formed Electrified Power Business Unit in the development of the first Cummins UK Module and Pack Battery designs for North American

Bus market. His research interests include Electrical Machine design, Mechanical Integration challenges and the prototyping of Inverters, Electrical Machines and Geared Traction Drive Systems.



Emil Ernest received the Ph.D. degree in specialization of Motion Control and Power Electronics with DSP microprocessor control system, Warsaw University of Technology, Poland, in 2006. He started his career in UK joining company NEWAGE AVK and later on as part of global company CUMMINS Ltd (2006-2022). His work concentrates on development and exploratory of Inverter hardware & control design for high-speed electrical machine and to support traction drive application. As a current role of Technical Advisor,

he continuously supports different power electronics solution and innovative technologies



Shaohong Zhu received his Ph.D. in Electrical and Electronic Engineering from The University of Nottingham, UK, in 2021, where he was an Early-Stage Marie Sklodowska-Curie Research Fellow from 2016 to 2019 working on developing modular electric actuators for More Electric Aircraft (MEA). He is currently an Electric Machine Engineer in Cummins Electrified Power Europe Limited, working on the development of electric powertrain systems for Heavy Duty Commercial Vehicles. His research interest includes design and analysis of high-speed

high power electric machines, optimization techniques, and fault-tolerant PM synchronous motors.



Naila Qayyum received her master degree in Embedded System and Control Engineering from university of Leicester, UK. She joined research and Technology department of Cummins in 2018. She worked on prototyping power electronics inverter solutions for traction application. She has worked on controlling of high-speed electrical machines, testing and validating electrical machine performance in test cell environment. Her research interests include developing efficient motor control algorithms including field oriented control, model predictive

control, optimized data sampling for feedback control, impact of variable switching frequency and modulation methods for high-speed machines operation.



Alastair McQueen obtained the master's degree in Engineering Design from The University of Huddersfield, UK in 2001. He started his career at Cummins in 1998 as an Aftermarket Engineering placement student with Cummins Turbo Technologies. Within Cummins, Alastair held several roles at CTT in Project Engineering, Service, Application Engineering, Technical Project Leadership, Programme Management and Programme Leadership. He currently leads engineering as the Global Technical Director, leading

teams in the UK, Romania, India, China and US at Cummins Generator Technologies.



Fengyu Zhang received B.E degree in thermal engineering from Huazhong University of Science and Technology, Wuhan, China in 2014 and Ph.D. degree in electrical machines from University of Nottingham, UK in 2019. She is currently a Senior Research Fellow in the area of thermal management on electrical machines within the PEMC group at University of Nottingham. Her main research interests include high performance motors for transport applications and their multi-domain optimization.



Chris Gerada received the Ph.D. degree in numerical modelling of electrical machines from the University of Nottingham, Nottingham, U.K., in 2005. He is currently an Associate Pro-Vice-Chancellor of Industrial Strategy and Impact and a Professor of Electrical Machines with the University of Nottingham, UK. He has secured over £20M of funding through major industrial, European, and U.K. grants and authored more than 350 referred publications. His principal research interest lies in electromagnetic energy conversion in electrical

machines and drives, focusing mainly on transport electrification. Prof. Gerada was awarded a Research Chair from the Royal Academy of Engineering in 2013.